Published in final edited form as:
Biochemistry. 2012 January 10; 51(1): 172–186. doi:10.1021/bi2015629.

A "Sliding Scale Rule" for Selectivity between NO, CO and O_2 by Heme Protein Sensors[#]

Ah-Lim Tsai[1], **Vladimir Berka**[1], **Emil Martin**[2], and **John S. Olson**[3]

[1]Division of Hematology, Internal Medicine, University of Texas Houston Medical School, Houston, TX, USA

[2]Division of Cardiology, Internal Medicine, University of Texas Houston Medical School, Houston, TX, USA

[3]Department of Biochemistry and Cell Biology, Rice University, Houston, TX. USA

Abstract

Selectivity between NO, CO, and O_2 is crucial for the physiological function of most heme proteins. Although there is a million-fold variation in equilibrium dissociation constants (K_Ds), the ratios for NO:CO:O_2 binding stay roughly the same, 1:~10^3:~10^6 when the proximal ligand is a histidine and the distal site is apolar. For these proteins, there is a "sliding scale rule" for plots of log K_D versus ligand type that allows predictions of K_D values if one or two are missing. The predicted K_D for O_2 binding to *Ns* H-NOX coincides with the value determined experimentally at high pressures. Active site hydrogen bond donors break the rule and selectively increase O_2 affinity with little effect on CO and NO binding. Strong field proximal ligands such as thiolate, tyrosinate and imidazolate exert a "leveling" effect on ligand binding affinity. The reported picomolar K_D for NO binding to sGC deviates even more dramatically from the sliding scale rule, showing a NO:CO K_D ratio of 1: ~10^8. This deviation is explained by a complex, multi-step process, in which an initial low affinity hexacoordinate NO complex with a measured $K_D \approx 54$ nM, matching that predicted from the sliding scale rule, is formed initially and then converts to a high affinity pentacoordinate complex. This multi-step 6c to 5c mechanism appears common to all NO sensors that exclude O_2 binding in order to capture lower level of cellular NO and prevent its consumption by dioxygenation.

The main biological functions of heme proteins are transport, storage, sensing of key diatomic gaseous molecules and participation in redox reactions (1, 2). The high reactivity of ferrous heme iron with dioxygen (O_2) to produce radicals precludes its presence as a free form in biological systems to avoid adverse reactions that lead to oxidative stress. Thus, in most cells free heme is either quickly integrated into proteins or rapidly degraded via the heme oxygenase pathway. The protein not only sequesters the Fe-protoporphyrin ring, but

[#]This work was supported by grants from NIH NHLBI grants HL095820 (A.-L.T), HL088128 (E. M.), HL047020 (J.S.O.) and NIGMS grant GM035649 (J.S.O.); the American Heart Association, South Central Affiliate Grant-in-Aid 09GRNT2060182 (E. M.), and The Robert A. Welch Foundation Grant C-0612 (J.S.O.).

Corresponding author: Ah-Lim Tsai, PhD, Division of Hematology, Internal Medicine, University of Texas Houston Medical School, MSB 5290, 6431 Fannin, Houston, TX, 77030. Phone: 713 500-6771, fax: 713 500-6810, Ah-lim.tsai@uth.tmc.edu.

Supporting Information Available

There are five tables (Table S1 – S5) and three figures (Figs. S1 – S3) in the Supporting Information. Tables part includes binding parameter values for NO, CO and O_2 of Mb single mutants (Table S1), other globins (Table S2), heme proteins containing a thiolate proximal ligand (Table S3), heme proteins containing a proximal imidazolate ligand (Table S4) and a panel of picket fence, pocketed, strapped, and capped heme models (Table S5). Figures part contains the correlational plots between binding parameters and ligand types for the Mb double mutants (Fig. S1), triple mutants (Fig. S2) and peroxidases with imidazolate proximal ligand (Fig. S3). This material is available free of charge via the Internet at http://pubs.acs.org.

also provides specific axial ligands, steric constraints, and electrostatic interactions that regulate exogenous ligand affinity, heme-iron redox potential, and the metal spin state.

Various protein structures have evolved to modulate the intrinsic selectivity of pentacoordinate heme-His complexes for the three major gaseous ligands, nitric oxide (NO), carbon monoxide (CO), and O_2, which differ by only one valence electron between the CO/NO and NO/O_2 pairs. The oxygen storage and delivery proteins, Mb and Hb, use "electrostatic" discrimination to preferentially stabilize bound O_2 by hydrogen bond donation from distal amino acids, normally histidine, tyrosine, or glutamine (3). In the NO-storing nitrophorins from the saliva of blood-sucking insects, the heme is present in the oxidized form, Fe(III)-protoporphyrin IX, which cannot bind either CO and O_2, but does permits a pH-dependent reversible uptake of NO and displacement by histamine (4). In the case of FixL, the oxygen sensor found in nitrogen fixing bacteria, the partial negative charge on bound O_2 induces inward movement of a key Arg220 to form a favorable electrostatic interaction. This conformation change triggers signaling and cannot be achieved by either NO or CO binding because the resulting Fe(II)-ligand complexes lack the strong polarizability of the $Fe(II)^{\delta(+)}$-$O_2^{\delta(-)}$ complex (5). The CO-sensing protein CooA from phototropic bacteria achieves CO-selectivity using a reversible redox switch mechanism. In contrast, O_2 binding to CooA causes rapid autooxidation to Fe(III) heme and superoxide formation, and NO binding leads to dissociation of the proximal ligand. Neither of these latter events trigger signal transduction (6).

The major target for NO signaling in mammals is sGC, which binds NO, ruptures the proximal Fe-His bond and triggers activation of cGMP formation. CO binding is weak and not capable of breaking the Fe-His coordination, whereas O_2 simply does not bind to reduced sGC (7). Most remarkably, sGC manages to bind NO with an apparent K_D of ~ 4×10^{-12} M (Table 1) (8) but excludes O_2, a property that has not been explained mechanistically. We have addressed this property of sGC quantitatively by defining the general rules that govern ligand selectivity in heme proteins with a neutral proximal histidine-Fe(II) bond. The deviation of the NO binding properties of sGC from these rules requires a multi-step binding mechanism, which explains how GC and Heme-Nitric oxide and OXgen binding (H-NOX) classes of heme-based protein sensors evolved such remarkably high selectivity for NO and against O_2.

To verify the general rules and the multi-step mechanism for the NO sensors, we reexamined the first step in NO binding to sGC and re-evaluated the ligand binding properties of a panel of heme-based protein sensors, globins, and model heme. The almost linear relationship of log K_D for NO versus CO versus O_2 binding for most heme proteins suggests a "sliding scale rule", which allows a prediction of the affinity of one ligand if K_D for the other ligand(s) is known. Deviations from this sliding scale rule are the result of stereochemical interactions with the surrounding protein elements that enhance selectivity in favor of one of the gaseous ligands and sometimes against the others.

METHODS

Construction of expression vector for His-tagged *Ns* H-NOX

The H-NOX of *Nostoc sp* PCC 7120 (*Ns* H-NOX^{-189}) gene sequence (GenBank Accession No. GI: 17229770) was first optimized for *E. coli* codon usage, replacing several rare codons with high-frequency synonymous codons to form a synthetic gene encoding *Ns* H-NOX. This optimized cDNA, together with six histidine codons inserted upstream of the stop codon (resulting in recombinant *Ns* H-NOX with a C-terminal His-tag), was synthesized and cloned into pBSK vector (Epoch LifeScience, Houston). The *Ns* H-NOX cDNA was released by digesting with NdeI and XhoI and subcloned into pET43.1a (pre-

digested by NdeI and XhoI). The integrity of the resulting plasmid, designated pET43.1a-*Ns* H-NOX, was confirmed by restriction digestion and DNA sequencing.

Expression and purification of His-tagged recombinant *Ns* H-NOX, sGC and prostacyclin synthase (PGIS)

The *E. coli* C43(DE3)pLysS strain (Lucigen, Middleton, WI) was transformed with the pET43.1a-*Ns* H-NOX expression plasmid and grown overnight in Terrific Broth medium containing chloramphenicol (45 μg/mL) and ampicillin (150 μg/mL) at 37 °C. The overnight culture (20 mL) was used to inoculate 1 L of Terrifc Broth containing ampicillin (150 μg/mL) and incubated with shaking (200 rpm) at 37 °C until the A_{610} reached 0.8. After chilling to 20 °C, heme (2 μM), δ-aminolevulinic acid (0.2 mM), and isopropyl-1-thio-β-D-galactopyranoside (IPTG, 1 mM) were added, and culture was continued for 48 h at 18 °C with shaking at 200 rpm. Cells were harvested by centrifugation and stored at −76 °C.

Cells from 2 liters of culture were resuspended in 125 mL of Buffer A (100 mM potassium phosphate, pH 7.5, 100 mM NaCl, 10% glycerol, and 1 mM β-mercaptoethanol). Egg lysozyme (150 mg in 5 mL of buffer A) was added and the suspension stirred at 4 °C for 1 h and then sonicated (10 min total; 10 s intervals, 50% duty cycle), then centrifuged at 100,000*g* at 4 °C for 1 h. A 10-mL portion of TALON affinity resin was packed in a glass column (2.8 × 23 cm) and washed with 10 vol of deionized water and 10 vol of Buffer A. The cleared cell lysate containing recombinant *Ns* H-NOX was then added to the column, and the mixture agitated gently for 2 h at 4 °C on a rotating mixer. The liquid was then drained from the column and the resin washed twice by capping the ends and agitating with 10 vol of Buffer A for 15 min. Then, two similar wash steps were performed with 10 vol of Buffer A containing 5 mM imidazole. The His-tagged *Ns* H-NOX was eluted with 5 vol of Buffer A containing 250 mM imidazole, and collected in 3 mL fractions. Fractions containing purified *Ns* H-NOX (based on the A_{418}/A_{280} ratio) were pooled and concentrated with a 30 kDa cutoff Centricon device. The concentrated *Ns* H-NOX was chromatographed on a 10-DG column pre-equilibrated with Buffer A to remove imidazole, and stored at −76 °C.

Soluble guanylyl cyclase (sGC), with a specific activity of 13.5 μmol cGMP/min/mg sGC was prepared in 50 mM triethanolamine, pH 7.5 (TEA), as previously described (9). The purified enzyme is 5c ferrous (A_{431} = 110 $mM^{-1}cm^{-1}$) and is inert to oxygen.

The recombinant human PGIS was prepared as described previously (10) with minor modifications in protein purification (11). Briefly, the human PGIS cDNA was modified by replacing the hydrophobic amino-terminal segment of the first 17 residues with a seven-residue segment (MAKKTSS) favoring expression in E. coli, and by adding a four-histidine tag at the carboxyl terminus. The modified cDNA was constructed in the pCW vector driven by *tac* promoter and recombinant PGIS was purified to electrophoretic homogeneity by nickel affinity column and CM-Sepharose column chromatography from which PGIS was eluted by 20 mM NaPi, pH 7.2, containing 150 mM NaCl and 10 % glycerol. Purified PGIS was stored at −70°C. Protein concentration was spectrophotometrically determined using ε_{418} = 103 mM^{-1} cm^{-1}.

Determination of protein and heme content

Total protein was assayed with Bio-Rad *DC* protein assay kit using bovine serum albumin as the standard. Heme content was determined by the pyridine hemochrome method using a difference absorbance coefficient (556–538 nm) of 24.5 mM^{-1} cm^{-1}. All protein samples we used were checked to have a full complement of heme.

Electrophoretic and immunoblot analyses

Protein samples were prepared by mixing with electrophoresis sample buffer containing 4.3% SDS and 250 mM dithiothreitol and incubation for 2 at 95 °C. Protein mixtures were separated by electrophoresis under denaturing conditions using 12% polyacrylamide gels, with the protein bands either visualized by Coomassie blue staining.

Anaerobic sequential stopped-flow

We determined k_{off}(NO) with an Applied Photophysics model SX-18MV stopped-flow instrument with a rapid-scan diode-array accessory. The sample handling unit was located inside an anaerobic chamber (Model 110V, Coy Laboratory Products, Inc.) filled with 10% H_2 in N_2 and fitted with a palladium-based O_2 scrubber. A gas analyzer (Model 10, Coy Laboratory) tracked both the hydrogen and oxygen level to make sure that the latter is 0 ppm during the kinetic measurements. sGC solution was prepared in an anaerobic glass titrator via 5 cycles of vacuum and argon replacement (30 s and 5 min, respectively). 2 mM NO stock solution and 1 mM CO stock solution in TEA buffer were prepared in glass tonometers by first saturating with pure nitrogen and then NO (or CO) at 1 atm. The opening of the side arm of the tonometers were then sealed with a rubber septum and transferred into the anaerobic chamber. Airtight disposable syringe with needle was used to retrieve different amount of NO stock solution to prepare the NO solution used for kinetic measurements. Other details of the kinetic measurements are given in the main text and legend of Fig. 2.

Determination of O_2 binding affinity for *Ns* H-NOX and sGC under high pressure

The custom-built pressure cell was equipped with anti-reflection coated sapphire windows and had a path length of 1 mm as previously described (12). In these experiments 200 μl of ferrous form of *Ns* H-NOX (50 μM) or sGC (10 μM) was added in the pressure cell that was pre-flushed with pure oxygen and isolated from air by screw metal joint, and then engaged to the oxygen cylinder by a control valve. Oxygen pressure was varied from 0 to 135 psi (or 9.2 atm) at 20 psi increments. Optical spectra were recorded after each increment of oxygen pressure and ~2 min equilibration by shaking the pressurized cell. After 135 psi, the cell was open to the air pressure and the spectrum was taken to check the reversibility..

EPR spectroscopy

Liquid helium temperature EPR spectra were recorded on a Bruker EMX spectrometer using a GFS600 transfer line and an ITC503 temperature controller. An Oxford ESP900 cryostat was used to accommodate the quartz sample tube in a ER 4116DM resonator (13). The conditions for liquid helium (10 K) EPR measurements were: frequency, 9.6 GHz; modulation amplitude, 10 G; modulation frequency, 100 kHz; and time constant, 0.33 s.

RESULTS

Linear logarithm plots of K_D(NO), K_D(CO) and K_D(O_2) for heme proteins with a neutral proximal histidine

Logarithmic plots of equilibrium dissociation constants (K_D), association (k_{on}) and dissociation (k_{off}) rate constants against ligand type were constructed for a large series of ferrous heme proteins that contain a neutral proximal histidine ligand (see Figs. 1, 5–8, and S1–S3). In Fig. 1, the K_D values for NO, CO, and O_2 binding to 5c (Fe(II)PP(1-MeIm)) (14–16), Mb (17–19), sGC (8, 9, 20–22), cytochrome c′ (cyt c′) (23–27) and HemAT (28) were taken from the literature, and those for sGC containing the I145Y mutation in the β subunit (αβI145Y sGC) (9), and *Ns* H-NOX (13) were determined in our laboratory (Table 1). NO always shows the highest affinity (lowest K_D) due to its radical nature and some back bonding, CO shows an intermediate affinity due to extensive back bonding, and O_2 shows

the lowest affinity because only a sigma bond can be formed with the iron atom (29–31). Although the absolute values of K_D vary over a million-fold, *i.e.* 6 units along the y-axis in Fig. 1, the K_D ratios of the CO/NO and O_2/CO pairs for each sample remain $10^3 – 10^4$. This trend is shown most clearly for the Fe(II)PP(1-MeIm) heme model (thick line and small black circles, Fig. 1) and leads to a "sliding " set of parallel lines for the NO to CO to O_2 series for most of the proteins that have been examined.

Major exceptions to the linear log plots are observed when hydrogen-bonding donors are present in the active site, resulting in preferential stabilization of bound O_2 and smaller $K_D(O_2)$ values from those predicted by the sliding scale rule (3, 18). This effect is seen most clearly by the lower than expected $K_D(O_2)$ for wild type sperm whale myoglobin (swMb) with a distal histidine compared to the higher value for H64V Mb in which the active site is apolar (Fig. 1, cyan vs. red circles) (32). However, the K_D ratios for CO/NO are relatively unchanged for these Mb variants. Similarly, in HemAT the distal tyrosine stabilizes bound O_2, and when it is replaced by phenylalanine, the apolar HemAT mutant shows a log K_D plot perfectly parallel with those for H64V Mb and the model heme (Fig. 1, blue vs. red triangles).

Thus, for gas-binding heme proteins in the reduced, Fe(II) state there appears to be a "sliding scale rule", which prescribes parallel lines for plots of log K_D for the series NO to CO to O_2. This relationship appears to apply to all 6c heme proteins and model hemes with a neutral proximal histidine ligand, and any decrease in the $K_D(O_2)/K_DCO$) ratio is readily explained by preferential electrostatic stabilization of the polar Fe-O_2 complex. All other protein structural effects, including direct hindrance of the bound ligand, water displacement from the active site, and proximal constraints of iron-His movements into and out of the plane of the heme, apply uniformly to the binding of all three ligands (33). The only major exception to this rule is the remarkably large $K_D(CO)/K_D(NO)$ ratio ($\sim 10^7 – 10^8$) for equilibrium binding to sGC. This ratio is 4 to 5 orders of magnitude bigger than that found for all the other heme proteins which have been examined (Figs. 1, 7–9 and S1–S3). The binding of CO to sGC is very weak ($K_D \approx 3 \times 10^{-4}$ M) and no O_2 binding to this protein has been detected. Thus, the predicted K_D for NO binding to form a ferrous 6c complex is $\sim 3 \times 10^{-7}$ to 10^{-8} M based on the sliding scale rule. In contrast, the reported $K_D(NO)$ value based on the ratio of published k_{on} and k_{off} values is 10^{-12} M. This deviation from the sliding scale rule is a consequence of the multi-step mechanism for NO binding to sGC to form a 5c NO-heme complex, as first suggested by Traylor and Sharma (references (8, 34, 35)).

Measurements of k_{on} and k_{off} of first NO binding step for sGC at ambient temperature

The k_{off} reported in the literature for NO dissociation from sGC refers to dissociation of the 5c NO-Fe(II) heme complex in its final equilibrium state (D in Scheme 1) and not to the labile 6c NO-Fe(II)-His complex transiently formed in the first-step of NO binding (8, 34) (C in Scheme 1). The $k_{off}(NO)$ values for the model heme, all the Mb variants, and the other heme proteins in Table 1 (and Figs. 5–7, S1, and S2) represent the rate of dissociation from *bona fide* 6c NO complexes. The k_{off} values for initial 6c NO-Fe(II)-His complexes can be reliably measured for cyt c′ (24, 25), αβI145Y sGC (9) and *Ns* H-NOX (13) (Table 1), because in these proteins the initial 6c NO complex is relatively stable and only slowly and partially converts to 5c NO-Fe(II) complexes at low [NO]/heme ratios.

To resolve the dilemma of the abnormally large $K_d(CO)/K_d(NO)$ of sGC, we determined both the on and off rate constants for the first step of NO binding to sGC at 24° for comparison with the rate constants listed in Table 1, most of which were measured near room temperature. Because the k_{on} value is very large (8), we had to conduct the kinetic measurements under 2nd-order conditions, using sGC:NO = 1:1 and a final concentration at 0.5 μM each, to avoid missing most of the time course in the dead time of the stopped-flow

apparatus. Measurements performed using either a rapid-scan diode array (Fig. 2) or single-wavelength detection (Fig. 2, Inset) captured more than 60% of the total expected changes. The observed time courses were fitted to a second order, irreversible mechanism (dashed line in Fig. 2 Inset) and yielded a value of $k_{on} = 4.8 \times 10^8\ M^{-1}s^{-1}$ which is similar to the previously reported value of $1.8 \times 10^8\ M^{-1}s^{-1}$ measured 4 °C (8).

To accurately measure k_{off} for the initial 6c NO-sGC complex with a Soret peak at 420 nm, we maximized its formation in sequential stopped-flow mixing experiments. The 6c NO complex was generated by reacting 2 μM sGC with 2 μM NO in the first mixing step. The conversion of Fe(II) sGC to NO-Fe(II)-His (A ↔ B in Scheme 1) was almost complete in the dead time of the stopped-flow apparatus (Fig. 3A). This initial NO/sGC mixture was aged for 15 – 200 ms and then being reacted with 1 mM CO and 25 mM dithionite to displace and consume dissociated NO, respectively (B → E in Scheme 1). After the second mixing step, an exponential increase in absorbance at 424 nm was observed, indicating formation of the CO-Fe(II)-His complex (E in Scheme 1) with a rate of ~ 27 s^{-1} (Fig. 3B). Increasing the aging time of the original 1:1 sGC:NO mixture up to 200 ms led to little variation in the total absorbance change, the final peak position, or the rate of NO displacement (Inset of Fig. 3B). However, in each case a small conversion to a 5c NO-Fe(II) complex with a lower intensity peak at 399 nm (a species similar to D in Scheme 1 but with NO sit on the distal site of the heme iron) occurs before the 6c NO-Fe(II)-His intermediate is maximally formed. If the same sGC sample, is reacted with an excess of NO, a final equilibrium 5c NO-Fe(II) complex is formed rapidly with a 399 nm absorbance band (D in Scheme 1) and little evidence of the 6c intermediates. Reaction of this complex with 1 mM CO and 25 mM dithionite led to a markedly smaller rate of NO dissociation, which is roughly equal to that reported previously in the literature (i.e. ~ 10^{-4} s^{-1}) (36) (D → A in Scheme 1).

The k_{off}(NO) value of 27 s^{-1} for the initial 6c NO complex was used to calculate a K_D(NO) of 5.4×10^{-8} M for dissociation of the initial NO-Fe(II)-His complex (Table 1 and Fig. 1, green diamond). When this value for the NO-Fe(II)-His complex of sGC is used, the line connecting logK_D(NO) and logK_D(CO) becomes parallel with those for all the other heme proteins studied and a 3 to 4-order intrinsic separation of the sGC K_D values between the NO/CO and CO/O_2 pairs. Thus the sliding scale rule applies for 6c sGC complexes even though the absolute values of the K_Ds for each ligand are ~6 orders of magnitude larger than those for the model heme-imidazole complex.

Linear extrapolation from the log K_D values for NO and CO binding predicts a K_D of ~1 M for O_2 binding sGC (Fig. 1, green diamond with grey edge), which is three orders of magnitude higher than [O_2] in buffer saturated with 1 atm O_2 (Fig. 1, horizontal red dash lines). Thus, when the 6c sGC complexes are examined, the “sliding scale rule” predicts the exclusion of oxygen binding by sGC, and similar empirical predictions can be made for O_2 binding to I145Y sGC, cyt c′, and *Ns* H-NOX, where the initial 6c NO complexes are more easily examined.

A test of the sliding scale rule: O_2 binding to *Ns* H-NOX under high pressure

Ns H-NOX appears to be unable to bind O_2 but does slowly autooxidize, indicating weak interaction with O_2 (13). Extrapolation from the observed K_D(CO) for *Ns* H-NOX by a line parallel to the data for the other proteins in Fig. 1 (pink circle with grey edge) predicts that the $K_D(O_2)$ for this sensor should be ~ 5 mM. If this sliding scale rule prediction is correct, then it should be possible to detect O_2 binding to *Ns* H-NOX spectrally using only moderately high O_2 pressures. Spectral changes for Fe(II) *Ns* H-NOX were observed in custom built pressure cell when the P_{O2} was increased from 0.2 atm to ~9 atm (130 psi). The Soret band changed from a 430 nm band typical of 5c Fe(II) heme to a broad band centered

at 424 nm, which is not the ferric form (Fig. 4A). The absorbance difference measured at 409 – 431 nm depends hyperbolically on [O_2] and was consistent in four different experiments. These data were analyzed with a simple one-step binding function, and the fitted K_D equals 13×10^{-3} M (Fig. 4, Inset) is close to the value predicted by the sliding scale rule (~5×10^{-3} M). In contrast, when the same experiment was tried with sGC, no change in Soret absorbance was observed, even at 9.2 atm of pure O_2, which is the highest limit before sample leakage from the pressure cell occurs.

The lack of a characteristic visible spectrum typical of HbO_2 complexes suggested that some oxidation might have occurred in the *Ns* H-NOX samples, particularly at 9 atm pressure of O_2. EPR spectra of samples withdrawn from the pressure cell were recorded to quantify the amount of iron oxidation (Fig. 4B). The oxygenated *Ns* H-NOX sample did show small signals for ferric heme at g = 6 (high-spin) and g = 3 and 2.25 (low-spin), and an increased amount of denatured hemin-protein complex represented by the g = 4.3 signal. However, the majority of the hemes were EPR-silent and present as either 5c Fe(II) or 6c Fe(II)O_2 complexes. Partial auto-oxidation and irreversible denaturation under treatment of high pressure O_2 was confirmed by failure to recover completely the original ferrous spectrum after the high O_2 pressure was released (data not shown). Nonetheless, it is clear that most of the original unliganded Fe(II) *Ns* H-NOX molecules do reversibly bind dioxygen with a K_D in the range of 5 to 10×10^{-3} M.

Characteristic dependences of log k_{on} and log k_{off} on ligand type

Correlation plots for the logarithms of k_{on} and k_{off} show more complex shapes as function of ligand type (Fig. 5). The log (k_{on}) plots show vertical displacements of a “V-shaped” pattern, with the bimolecular rate constant for CO binding showing the smallest value, which is almost always 100 to 1000-fold smaller than k_{on}(NO) and 10 to 100-fold smaller than k_{on}(O_2). As described by Champion, Franzen, Harvey, and their coworkers (37–40), the much smaller values of k_{on}(CO) are due to both the requirement of in-plane movement of the heme iron to vacate the electron in the d_{z2} orbital and the spin-forbidden nature of iron-carbonyl bond formation. As result, the rate-limiting step for CO binding is internal bond formation with the iron atom. In contrast, bond formation can occur without a spin-state change of the iron when NO and O_2 are the ligands, because both contain unpaired electrons (37–40). As result, the rate of internal bond formation is very rapid for these ligands, and in the case of NO binding, the rate-limiting step for bimolecular association is ligand migration into the active site. In the case of O_2 binding, k_{on} can be limited by both ligand migration and bond formation, depending on the reactivity of the iron atom and steric restriction near the active site (41). Thus, in most proteins $k_{on}(NO) \gg k_{on}(CO) < k_{on}(O_2)$ and a sliding V-shaped scale is seen (41).

The pattern for log(k_{off}) is less clear and shows much great variably in both the $k_{off}(CO)/k_{off}(NO)$ and $k_{off}(O_2)/k_{off}(CO)$ ratios. However, in general $k_{off}(NO) \leq k_{off}(CO) \ll k_{off}(O_2)$ so the pattern has characteristics of a “backward L.” In general, the rate constant for O_2 dissociation in heme proteins with an apolar active site is roughly 10^6-fold greater than that for CO dissociation and assuming this relationship holds for gas sensors, the predicted O_2 dissociation constant for sGC is estimated to be ~ 5×10^6 s^{-1} (Fig. 5, right panel, dashed line and green diamond with grey edge vs. red line and black circles). The $k_{on}(O_2)$ for sGC can then be estimated from this predicted k_{off} and the estimated K_D (~ 1 M) from Fig. 1. The resulting k_{on} value is ~ 2×10^6 $M^{-1}s^{-1}$ (Fig. 5, left panel, green diamond with grey edge), conforming well with the expected “V” shape for log(k_{on}) plots.

Are the sliding scale rules applicable to all globin variants?

Over the past twenty years, the biochemical mechanisms for NO, CO, and O_2 binding have been examined systematically for large libraries of mammalian Mb and Hb variants (3, 32, 33). As a test of the analysis in Fig. 1, we constructed a graphical analysis for NO, CO, and O_2 binding to eleven single Mb mutants, out of a panel of 42 for which we have complete binding parameter values (42–44). These 11 Mb mutants showed the largest changes in K_D, k_{on} or k_{off} compared to the wt Mb parameters. As shown in Fig 6a, the K_D(NO) and K_D(CO) values for these 11 mutants are highly correlated in the ranges, $10^{-10} – 10^{-12}$ and $10^{-7} – 10^{-9}$ M, respectively, showing parallel lines in the log plots.

In contrast, the log $K_D(O_2)$ values show significant deviations from the linear sliding scale rule. Marked decreases in $K_D(O_2)$ are observed for those variants with increased hydrogen bonding or favorable positive electrostatic fields, which preferentially stabilize bound O_2 (i.e. variants with His64 and Phe29). However, those Mb mutants with apolar distal pockets follow the expected linear sliding scale rule (Fig. 6A, thick blue lines). The y-axis positions of the logK_D values can be readily interpreted in terms of structural effects that regulate ligand affinity, all of which have been well established for Mb (3, 32) and are indicated by the arrows in Fig. 6. Lower iron reactivity due to proximal constraints of in-plane movement, direct steric hindrance at the active site, and water displacement from the distal pocket increase the K_D for the binding of all three gaseous ligands, whereas positive fields and hydrogen bond donors preferentially stabilize bound O_2, causing a downward deflection of the last log $K_D(O_2)$ points in the plots (Fig. 6A). Similar trends and explanations apply to all the other Mb variants that have been examined, and examples of these data are shown in Figs. S1A and S2A of the supplement for double and triple mutants.

Correlation plots for the bimolecular association (k_{on}) and unimolecular dissociation (k_{off}) rate constants for the same set of reduced Mb variants and are shown in Fig. 6B. The trends for log(k_{on}) are given in the left hand panel, and the “V-shape” is result of the differences in rate limiting steps. NO binding to ferrous deoxyMb is limited only by the rate of entry into the protein active site; CO binding is limited by bond formation; and O_2 binding is partially limited by both processes. The bimolecular rate of ligand entry is governed by displacement of distal pocket water, diffusion into the distal pocket, and the size of the internal capture volume, whereas the rate of bond formation is governed by the reactivity of the iron atom (proximal effects) and steric hindrance at the open axial position. In the case of CO binding, the overall expression for k_{on} is $k_{bond}K_{entry}$ where K_{entry} is the equilibrium constant for non-covalent ligand binding in the active site, which also depends on the need to displace distal pocket water and the active site volume (41). Thus, when iron reactivity is lowered by proximal effects or direct hindrance, the depth of the “V-shape” in the log(k_{on}) plot is greater due to little change in k_{on}(NO) but large decreases in k_{on}(CO). However, if the capture volume is decreased markedly as is the case for V68W Mb, all the rates are decreased dramatically and the “V-shape” is much more shallow because slow ligand capture becomes limiting for all three ligands (grey triangles, Fig. 6B, left panel).

The dominant variations seen in the log(k_{off}) plots are due to preferential electrostatic stabilization of bound O_2, causing dramatic decreases in the absolute value of $k_{off}(O_2)$ and the $k_{off}(O_2)/k_{off}$(CO) ratio (Fig. 6B, right panel). In contrast, decreases in Fe(II) reactivity and direct steric hindrance of the bound ligand cause increases in k_{off} for all three ligands. There is some variability for k_{off}(NO) because the Fe(II)NO complex can be stabilized weakly by hydrogen bonding (3, 45). Again, similar correlation plots and interpretations can be made for libraries of double and triple mutants of sperm whale Mb and the results all support the sliding scale rules (Figs S1 and S2)

As a more stringent test of the sliding scale analyses, we examined the ligand binding parameters for 11 different reduced globins from all kingdoms of life, including: the plant hemoglobins, leghemoglobin (Lb) (46) and rice hemoglobin 1 (rHb1) (47); the invertebrate Hb from *Ascaris suum* (Asc Hb) (19); flavohemoglobins (FHb) from bacteria and fungi; truncated Hbs (trHbs) from microorganisms including trHbN and trHbO from *Mycobacterium tuberculosis* and trCb, a single domain hemoglobin from *Campylobacter jejuni* (48); and human neuroglobin (Ngb) (49) (Fig. 7, Table S2). There is a much greater range of absolute values for all the rate and equilibrium parameters, but the same rules and interpretations apply. For some of these globins there are multiple hydrogen bonding interactions with bound O_2 leading to dramatic decreases in $K_D(O_2)$ and $k_{off}(O_2)$ and ratios for $K_D(O_2)/K_D(CO)$ and $k_{off}(O_2)/k_{off}(CO) \leq 1.0$ (i.e. *Ascaris* Hb, trHbO, trHbN, rHb1, and trCb). When the active site proton donors are replaced with apolar amino acids, the expected, linear, V-shaped, and reverse L-shaped plots are observed for $\log(K_D)$, $\log(k_{on})$, and $\log(k_{off})$, respectively (Fig. 7, thick blue lines). These data, coupled with those for the Mb libraries and the heme proteins shown in Fig. 1, argue strongly for the utility of the sliding scale analysis and its ability to predict ligand binding parameters if a set of K_D, k_{off}, and k_{on} parameters has been measured for CO binding and the polarity of the active site is known.

Heme proteins with a thiolate proximal ligand do not follow the sliding scale rule

There are limited and, in most cases, incomplete kinetic data for NO, CO, and O_2 binding to the reduced form of cytochrome P450 and P450-like proteins containing a proximal thiolate protein ligand. Nitric oxide synthase is the only one with a complete set of published binding parameters for all three ligands (50, 51) (Table S3) K_D and k_{on} values for only two gas ligands are available for Fe(II) P450cam (52–54), P450BM3 (54, 55), chloroperoxidase (CLP) (56, 57) and prostacyclin synthase (PGIS) (58, 59). The $k_{on}(NO)$ values for both P450cam and PGIS are $\gg 10^8\ M^{-1}s^{-1}$ (Van Eldik, Rudi, personal communication and our unpublished results, respectively) and cannot be determined by simple rapid-mixing methods; however, the $k_{off}(NO)$ values could be determined for these two proteins. The ferric P450cam-NO complex was reduced with excess $[Ru(EDTA)H_2O]^-$, and $k_{off}(NO)$ was determined to be $0.35\ s^{-1}$ (52). For PGIS, the ferrous protein was prepared by anaerobic titration with dithionite, and k_{off} was measured by sequential mixing, stopped-flow protocols, as described for measuring $k_{off}(NO)$ from the 6c NO complex of sGC (see Methods and Fig. 3). A delay time between 0.5 – 1 s allowed us to maximize formation of the Fe(II)NO complex formation before the ligand was displaced by mixing with 1 mM CO and 40 mM dithionite. The kinetics of CO dissociation from the ferrous PGIS-CO complex formation was determined to be $0.3\ s^{-1}$ at 24 °C by mixing with buffer equilibrated with 1 atm of NO (Fig. 8b, right).

Even with limited data, it is clear from Fig. 8a and Table S3, that the $\log(K_D)$ values for heme proteins with a proximal thiolate fail to follow the simple sliding scale rule observed for proteins with a proximal His (Figs 1, 5–7). There is little variation of the K_D values for all three ligands, and $K_D(O_2)$ is actually smaller than $K_D(CO)$ for P450cam, even though there are no polar residues in the active site to stabilize bound dioxygen (Table S3). Thiolate coordination seems to abolish ligand binding selectivity. With the exception of PGIS, the k_{on} values seem to still follow the “V” shape sliding scale rule (Fig. 8b, left panel), but the “reversed L” sliding scale relationship no longer holds for k_{off} values for P450-like heme proteins, for which there is a “leveling effect” causing the k_{off} values of all three ligands to be very similar (Fig. 8b, right panel).

Peroxidases also do not follow the sliding scale rules

We also analyzed data for five peroxidases, which have published binding parameters for at least two of the gas ligands (Table S4). These enzymes include horseradish peroxidase (HRP) (60, 61), lactoperoxidase (LPO) (62, 63), eosinophil peroxidase (EPO) (62), cytochrome c peroxidase (CcP) (64, 65) and myeloperoxidase (MPO) (62, 66). In these proteins, the anionic imidazolate form of the proximal His side chain is coordinated to the iron atom due to the presence of ionized Asp and Glu side chains (67). Plots of $\log(K_D)$ against ligand type for these enzymes show little variation and look similar to those for the P450-like heme proteins with a thiolate axial ligand (Fig. S3a). The $\log(k_{on})$ values still show a "V" shaped dependence but are clustered in a very narrow range for all three k_{on} parameters with values that are about 3 orders lower than those for the chelated model heme (Fig. S3b, left). The $\log(k_{off})$ plots show both $k_{off}(NO)$ and $k_{off}(O_2)$ values that are greater than those for $k_{Off}(CO)$, a behavior that is different from heme proteins with a neutral proximal imidazole axial ligand and the P450-like proteins with a thiolate ligand. More work is needed to understand the structural and chemical bonding mechanisms that regulate gas binding to the latter two classes of heme proteins.

DISCUSSION

Utility of the sliding scale analysis for understanding ligand discrimination

Reduced pentacoordinate heme proteins with a neutral proximal histidine show innate chemical discrimination between NO, CO, and O_2, just like the Fe(II)-Imidazole heme model, even though the absolute affinities for any specific ligand can vary over a million-fold (Fig. 1). Extensive back bonding from the exogenous ligand to the iron d orbitals is allowed by the neutral axial imidazole, and coupled with the radical nature of NO, causes the K_D for NO binding to be roughly 10^{-3} to 10^{-4}-fold smaller than that for CO binding, which in turn is 10^{-3} to 10^{-4}-fold smaller than that for the binding of O_2, which lacks capability of back bonding. Thus, plots of $\log(K_D)$ versus ligand type for the series NO, CO, and O_2 are roughly linear and parallel for a wide variety of heme models and proteins which have apolar active sites and a neutral proximal histidine (Figs. 1, 6, and 7). Studies of ligand binding parameters for synthetic model hemes designed to modulate the steric and electrostatic interaction seen in proteins are sporadic and incomplete (14–16, 68–72) (Table S5). We could not find another model heme compound, containing a proximal imidazole ligand, for which binding kinetic studies had been conducted for all three gases. Most experiments only examined O_2 and CO binding (e.g. (68)) and were limited for compounds containing a proximal imidazole base (14–16, 71, 72). However, the data that do exist show the general relationship: $K_D(O_2/K_D(CO) \approx 10^3 – 10^4$ for models with apolar distal regions and this ratio is relatively insensitive to the degree of steric hindrance as indicated by a series of heme models with picket fence, strapped, pocket and capped distal pocket (Table S5)(68, 71, 73–75). Only polar interactions or severe steric effect that led to substantial porphyrin nonplanarity led to a marked lowering of this ratio (68, 71, 73–75).

This linear relationship suggests a sliding scale along the y-axis of these plots and preservation of marked ligand discrimination, with the relative affinities always being NO $\gg$ CO $\gg$ O_2. Absolute affinity can be increased by facilitating or sterically pushing the proximal Fe-imidazole complex into the plane of the porphyrin ring to enhance the reactivity of the iron atom and/or by removing any steric constraints adjacent to the distal axial position. These structural effects in combination with the intrinsic chemical differences between the ligands lead to a remarkably wide range of ligand affinities, from 10^{-13} to almost 1 M (Figs. 1 and 7). This combination of ligand discrimination coupled with a much wider range of possible ligand binding affinities accounts for why gas sensor, storage, and transport heme proteins maintain the neutral form of the proximal imidazole.

In contrast, when the proximal ligand is a thiolate (P450-like heme proteins) or an imidazolate (peroxidases), there is very little equilibrium discrimination between NO, CO, and O_2, and the range of absolute affinities is smaller, with K_D values ranging from 10^{-7} to 10^{-3} M. Thiolate is a very strong field ligand and highly electron-donating. As result, there is strong competition for back bonding to the Fe(II) d_z^2 orbital with the distal gaseous ligand (31). This competition with the thiolate exerts a "leveling" effect between NO, CO, and O_2 and, in general, decreases the Fe-XO bond strength and increases both the K_D and k_{off} for all three gaseous ligands (Fig. 8). Similar interpretations apply to peroxidases containing a proximal imidazolate ligand (Fig. S3). HRP, LPO, CcP, ascorbate peroxidase, lignin peroxidase, and peanut peroxidase all have a proximal histidine with imidazolate character due to H-bonding interactions with nearby proton-bond acceptors (Asp or Asn) (67). These peroxidases all have negative midpoint potentials, and the strong electron donating or pushing effect by the imidazolate helps promote heterolytic cleavage of the O-O bond of bound peroxide, but at the expense of much weaker discrimination between the gaseous ligands and higher K_D values. Although crystallographic data for EPO are not available and MPO has an abnormally high midpoint potential and weak affinity for CO, biophysical studies have demonstrated that both peroxidases still have an imidazolate, proximal ligand (67), accounting for their lack of discrimination between the gaseous ligands.

The sliding scale rule is also useful for predicting K_D values that are difficult or impossible to measure experimentally. Several NO sensing heme proteins show very little or no reactivity toward O_2, making it difficult to even estimate $K_D(O_2)$. However, it is straightforward to measure $K_D(CO)$ values for these proteins (Table 1, Fig. 1). If the sliding scale rule applies, the slopes of $\log(K_D)$ vs. ligand plots for model hemes or other proteins can be used to predict $K_D(O_2)$ for the NO sensors. This analysis was done in Fig. 1 for *Ns* H-NOX and sGC, and the predicted K_D values are ~0.005 and ~1 M, respectively. As shown in Fig. 4, O_2 binding to *Ns* H-NOX can be observed at high pressures, and the fitted value for $K_D(O_2)$ was ~0.010 M, which on a logarithmic scale is very close to the predicted value and verifies the utility of the sliding scale rule. The value for sGC shows that it would require ≥ 100 atm of pure O_2 to see any binding at all (i.e. ≥10 % saturation), which accounts for why no O_2 binding has been observed and autooxidation occurs in days.

The sliding scale rule can also be used to predict $K_D(NO)$ values of ~10^{-8} and ~10^{-10} M for sGC and *Ns* H-NOX, respectively, based on the measured $K_D(CO)$ values for these NO sensors. Again, the predicted value for *Ns* H-NOX agrees well with that measured for the formation of the first 6c NO complex (13), verifying our analysis. In contrast, the reported K_D for NO binding to sGC is ~1×10^{-12} M, which is almost 10,000 fold smaller than the predicted value. However, the final sGC form is a 5c NO-heme complex with the proximal imidazole displaced. Thus, both the lack of correlation with the sliding scale rule and the change in proximal coordination geometry indicate a complex, multiple step mechanism for NO binding to sGC. Nonetheless, as shown in Figs. 2 and 3, the first NO binding step to form a transient 6c NO-heme-neutral imidazole complex shows a K_D of 5×10^{-8} M, which is remarkably close to the value predicted from the sliding scale rule and again verifies the utility of the sliding scale analysis.

Oxygen sensor, storage, and transport heme proteins

Specific high affinity O_2 binding requires significant deviation from the sliding scale rule in order to both alter ligand discrimination and decrease $K_D(O_2)$ values into the micromolar range for sensing, transport, and storage and to the nanomolar range for O_2 scavenging without oxidation. As described in previous work (32, 76), selective increases in O_2 affinity are achieved by increased positive electrostatic fields adjacent to the Fe-O_2 complex and direct hydrogen bonding. As shown in Figs. 1, 6, and 7, these favorable polar interactions can decrease the $K_D(O_2)/K_D(CO)$ ratio from ~10,000 for apolar active sites to ≤ 1.0 in

proteins where multiple hydrogen bonds are donated to bound O_2. The best example of a heme protein with a nanomolar $K_D(O_2)$ and little or no CO binding is the domain 1 hemoglobin of *Ascaris suum*, which is an obligate anaerobe in its adult stage and requires this globin to protect itself from O_2 poisoning (Fig. 7 and (19)). The sliding scale rule analyses in Figs. 6 and 7 provide a concise way of quantifying and comparing the effects of distal pocket polarity on discrimination in favor of O_2 binding.

NO sensors and discrimination against NO dioxygenation

In the case of NO sensors, the problem is not equilibrium ligand discrimination. All proteins with a neutral proximal histidine and an apolar distal pocket have much higher affinities for NO than either CO or O_2. Even in air (2.5×10^{-4} M O_2) and low 10^{-9} M levels of NO, the $K_D(O_2)/K_D(NO)$ ratio of 10^8 still favors reversible NO binding. The dilemma is NO dioxygenation by bound O_2, which destroys the signaling molecule. In air and low levels of NO, O_2 will kinetically out-compete NO for initial binding to 5c Fe(II) unliganded heme protein sensors because the values of $k_{on}(O_2)$ are normally only slightly smaller than those for $k_{on}(NO)$ (Figs. 5–7). Then NO will react rapidly with the newly formed O_2-heme-imidazole complex to produce nitrate with a bimolecular rate constants roughly equal to that for simple NO binding to the unliganded protein (77, 78). Thus, for a NO sensor to remain functional under aerobic conditions, it has to completely exclude O_2 binding to prevent NO dioxygenation. This requirement has been achieved in *Ns* H-NOX, cyt c′, and sGC by combinations of proximal restrictions and steric hindrance of the bound ligand, both of which markedly reduce ligand affinity. However, these structural effects also markedly increase the K_D for NO binding to form a conventional 6c NO-heme-imidazole complex (Scheme 1 for sGC). Based on the sliding scale rule, the CO binding parameters for sGC predicts a $K_D(NO)$ value in the 10^{-8} M region which is too high for sensing nanomolar levels of the gas. Thus, sGC has evolved a complex multi-step reaction mechanism in which the initial 6c NO complex converts to a high affinity 5c complex by displacement of the proximal imidazole, a process that is accelerated by additional NO molecules (Scheme 1, (27, 79)). The net result is a picomolar NO affinity for sGC and total exclusion of O_2 binding even under aerobic conditions. Similar multi-step NO reactions and O_2 exclusion were also observed for cyt c′, which shows high selectivity for NO. In this protein, O_2 binding is excluded by distal steric hindrance from L16 side chain (26, 27) rather than the proximal strain as shown for sGC.

The nitrophorin NO storing protein found in insect salivary glands has adopted an alternative mechanism for preventing O_2 binding and dioxygenation. Nitrophorins exist in the Fe(III) state, which excludes O_2 and CO binding, but can still bind NO, although with only micromolar K_D values. The high K_D facilitates rapid displacement of NO by histamine after injection into mammalian hosts, which induces vasodilation and inhibits inflammation at the same time. This strategy of using Fe(III) binding is effective for NO storage and rapid release at high concentrations but not for sensing nanomolar levels of NO as a cell signaling molecule.

Conclusions

Five coordinate Fe(II) heme proteins with a neutral proximal His ligand strongly discriminate between the gaseous ligands, with affinities being in the order NO ≫ CO ≫ O_2 due to differential effects of back bonding and spin coupling. There is a linear dependence of $\log(K_D)$ on ligand type for the NO, CO, and O_2 series, regardless of the absolute values for individual equilibrium dissociation constants. Deviations from this sliding scale rule do occur in heme proteins that function as relatively high affinity O_2 sensors, storage, and transport proteins and have active site amino acids which can donate hydrogen bonds to the bound O_2 molecule, and preferentially lower $K_D(O_2)$. Cytochrome P450-like proteins and

peroxidases contain strong-field proximal thiolate and imidazolate ligands, which assist in heterolytic O-O bond cleavage of the substrate but compromise their capability of discriminating between NO, CO, and O_2 binding. NO sensor proteins restrict the binding of all gaseous ligands by both proximal constraints of in-plane iron movement and direct hindrance of the bound ligand. These constraints effectively exclude O_2 binding. High affinity for NO is achieved by a second step in which an ultra stable 5c NO-heme complex is formed by displacement of the distal His. This multi-step mechanism appears to be a general strategy for all high affinity NO sensors that need to exclude O_2 binding to prevent dioxygenation of the signaling molecule.

Supplementary Material

Refer to Web version on PubMed Central for supplementary material.

Acknowledgments

We thank Dr. Lee-Ho Wang for providing us prostacyclin synthase sample for NO binding kinetic measurements; Dr. Wen Liu for establishing the expression system for *Ns* H-NOX and purified the recombinant protein for our oxygen binding experiment. We also wish to thank Professor Joseph Bonaventura for suggesting to try a high pressure cell O_2 binding to the sensors at the Gordon Research Conference on Nitric Oxide, 2011. Finally, we wish to acknowledge the strong influence that Vijay S. Sharma and Teddy G. Traylor had on our thinking about ligand discrimination and NO binding to heme proteins. Their ideas published and shared with one of us (J.S.O.) in the late 1980s were among the first to recognize the importance of distal pocket polarity in preferentially stabilizing bound O_2 in globins and formation of pentacoordinate NO-heme complexes in NO sensors.

ABBREVIATIONS

NO	nitric oxide
CO	carbon monoxide
O_2	dioxygen
DTT	dithiothreitol
β-BME	mercaptoethanol
IPTG	isopropyl-1-thio-β-D-galactopyranoside
cGMP	cyclic GMP
Mb	myoglobin
Fe(II)	ferrous heme
Fe(III)	ferric heme
5c-NO	five coordinate NO-heme complex
6c-NO	six coordinate NO-heme complex
Hb	hemoglobin
H-NOX	Heme-Nitric oxide and OXygen binding
***Ns* H-NOX**	*Nostoc sp* H-NOX
***Tt* H-NOX**	*Thermoanaerobacter tengcongensis* H-NOX
sGC	soluble guanylyl cyclase
αβI145Y sGC	sGC containing the I145Y mutation in the β subunit
cyt c′	cytochrome c′

CB	*Clostridium botulinum*
Lb	plant hemoglobins, leghemoglobin
rHb	rice hemoglobin
Asc Hb	invertebrate Hb from *Ascaris suum*
FHb	flavohemoglobins
trHbs	truncated Hbs
trHbN and trHbO	trHbs from *Mycobacterium tuberculosis*
trCb	a single domain trHb from *Campylobacter jejuni*
Ngb	neuroglobin
CLP	chloroperoxidase
PGIS	prostacyclin synthase
HRP	horseradish peroxidase
LPO	lactoperoxidase
EPO	eosinophil peroxidase
CcP	cytochrome c peroxidase
MPO	myeloperoxidase
EPR	electron Electron Paramagnetic Resonance spectroscopy

References and Notes

1. Messerschmidt, A.; Huber, R.; Poulos, T.; Wieghardt, K., editors. Handbooks of metalloproteins. Vol. 1. John Wiley and Sons, Ltd; Chichester: 2001.
2. Turano, P.; Lu, Y. Iron in heme and related proteins. In: Bertini, I.; Sigel, A.; Sigel, H., editors. Handbook on Metalloproteins. Marcel Dekker, Inc; New York, Basel: 2001. p. 269-342.
3. Olson JS, Phillips GNJ. Myoglobin discriminates between O2, NO, and CO by electrostatic interactions with the bound ligand. J Biol Inorg Chem. 1997; 2:544–552.
4. Walker FA. Nitric oxide interaction with insect nitrophorins and thoughts on the electron configuration of the {FeNO}6 complex. J Inorg Biochem. 2005; 99:216–236. [PubMed: 15598503]
5. Dunham CM, Dioum EM, Tuckerman JR, Gonzalez G, Scott WG, Gilles-Gonzalez MA. A distal arginine in oxygen-sensing heme-PAS domains is essential to ligand binding, signal transduction, and structure. Biochemistry. 2003; 42:7701–7708. [PubMed: 12820879]
6. Aono S. Biochemical and biophysical properties of the CO-sensing transcriptional activator CooA. Acc Chem Res. 2003; 36:825–831. [PubMed: 14622029]
7. Derbyshire ER, Marletta MA. Biochemistry of soluble guanylate cyclase. Handb Exp Pharmacol. 2009:17–31. [PubMed: 19089323]
8. Zhao Y, Brandish PE, Ballou DP, Marletta MA. A molecular basis for nitric oxide sensing by soluble guanylate cyclase. Proc Natl Acad Sci U S A. 1999; 96:14753–14758. [PubMed: 10611285]
9. Martin E, Berka V, Bogatenkova E, Murad F, Tsai AL. Ligand selectivity of soluble guanylyl cyclase: Effect of the hydrogen bonding tyrosine in the distal heme pocket on binding of oxygen, nitric oxide and carbon monoxide. J Biol Chem. 2006
10. Yeh HC, Hsu PY, Wang JS, Tsai AL, Wang LH. Characterization of heme environment and mechanism of peroxide bond cleavage in human prostacyclin synthase. Biochim Biophys Acta. 2005; 1738:121–132. [PubMed: 16406803]

11. Yeh HC, Tsai AL, Wang LH. Reaction mechanisms of 15-hydroperoxyeicosatetraenoic acid catalyzed by human prostacyclin and thromboxane synthases. Arch Biochem Biophys. 2007; 461:159–168. [PubMed: 17459323]
12. Scott EE, Gibson QH. Ligand migration in sperm whale myoglobin. Biochemistry. 1997; 36:11909–11917. [PubMed: 9305984]
13. Tsai AL, Berka V, Martin FE, Ma X, van den Akker F, Fabian M, Olson JS. Is Nostoc H-NOX an NO sensor or Redox Switch? Biochemistry. 2010
14. Rose EJ, Venkatasubramanian PN, Swartz JC, Jones RD, Basolo F, Hoffman BM. Carbon monoxide binding kinetics in “capped” porphyrin compounds. Proc Natl Acad Sci U S A. 1982; 79:5742–5745. [PubMed: 6957890]
15. Chang CK, Traylor TG. Reversible oxygenation of protoheme-imidazole complex in aqueous solution (1, 2). Biochem Biophys Res Commun. 1975; 62:729–735. [PubMed: 1120080]
16. Hoshino M, Ozawa K, Seki H, Ford PC. Photochemistry of nitric oxide adducts of water-soluble iron(III) porphyrin and ferrihemoproteins studied by nanosecond laser photolysis. J Am Chem Soc. 1993; 115:9568–9575.
17. Carver TE, Brantley RE Jr, Singleton EW, Arduini RM, Quillin ML, Phillips GN Jr, Olson JS. A novel site-directed mutant of myoglobin with an unusually high O2 affinity and low autooxidation rate. J Biol Chem. 1992; 267:14443–14450. [PubMed: 1629229]
18. Quillin ML, Li T, Olson JS, Phillips GN Jr, Dou Y, Ikeda-Saito M, Regan R, Carlson M, Gibson QH, Li H, et al. Structural and functional effects of apolar mutations of the distal valine in myoglobin. J Mol Biol. 1995; 245:416–436. [PubMed: 7837273]
19. Draghi F, Miele AE, Travaglini-Allocatelli C, Vallone B, Brunori M, Gibson QH, Olson JS. Controlling ligand binding in myoglobin by mutagenesis. J Biol Chem. 2002; 277:7509–7519. [PubMed: 11744723]
20. Stone JR, Marletta MA. The ferrous heme of soluble guanylate cyclase: formation of hexacoordinate complexes with carbon monoxide and nitrosomethane. Biochemistry. 1995; 34:16397–16403. [PubMed: 8845366]
21. Boon EM, Huang SH, Marletta MA. A molecular basis for NO selectivity in soluble guanylate cyclase. Nat Chem Biol. 2005; 1:53–59. [PubMed: 16407994]
22. Stone JR, Marletta MA. Spectral and kinetic studies on the activation of soluble guanylate cyclase by nitric oxide. Biochemistry. 1996; 35:1093–1099. [PubMed: 8573563]
23. Kassner RJ. Ligand binding properties of cytochromes c′. Biochim Biophys Acta. 1991; 1058:8–12. [PubMed: 1646027]
24. George SJ, Andrew CR, Lawson DM, Thorneley RN, Eady RR. Stopped-flow infrared spectroscopy reveals a six-coordinate intermediate in the formation of the proximally bound five-coordinate NO adduct of cytochrome c′. J Am Chem Soc. 2001; 123:9683–9684. [PubMed: 11572694]
25. Andrew CR, George SJ, Lawson DM, Eady RR. Six- to five-coordinate heme-nitrosyl conversion in cytochrome c′ and its relevance to guanylate cyclase. Biochemistry. 2002; 41:2353–2360. [PubMed: 11841228]
26. Antonyuk SV, Rustage N, Petersen CA, Arnst JL, Heyes DJ, Sharma R, Berry NG, Scrutton NS, Eady RR, Andrew CR, Hasnain SS. Carbon monoxide poisoning is prevented by the energy costs of conformational changes in gas-binding haemproteins. Proc Natl Acad Sci U S A. 2011; 108:15780–15785. [PubMed: 21900609]
27. Hough MA, Antonyuk SV, Barbieri S, Rustage N, McKay AL, Servid AE, Eady RR, Andrew CR, Hasnain SS. Distal-to-proximal NO conversion in hemoproteins: the role of the proximal pocket. J Mol Biol. 2011; 405:395–409. [PubMed: 21073879]
28. Zhang W, Olson JS, Phillips GN Jr. Biophysical and kinetic characterization of HemAT, an aerotaxis receptor from Bacillus subtilis. Biophys J. 2005; 88:2801–2814. [PubMed: 15653746]
29. Tsai AL. How does NO activate hemeproteins? FEBS Lett. 1994; 341:141–145. [PubMed: 8137931]
30. Spiro TG, Jarzecki AA. Heme-based sensors: theoretical modeling of heme-ligand-protein interactions. Curr Opin Chem Biol. 2001; 5:715–723. [PubMed: 11738184]

31. Spiro TG, Zgierski MZ, Kozlowski PM. Stereoelctronic factors in CO, NO and O_2 binding to heme from vibrational spectroscopy and DFT analysis. Coord Chem Rev. 2001; 219–221:923–936.
32. Phillips GN Jr, Teodoro ML, Li T, Smith B, Olson JS. Bound CO is a molecular probe of electrostatic potential in the distal pocket of myoglobin. J Phys Chem B. 1999; 103:8817–8829.
33. Coyle CM, Vogel KM, Rush TS 3rd, Kozlowski PM, Williams R, Spiro TG, Dou Y, Ikeda-Saito M, Olson JS, Zgierski MZ. FeNO structure in distal pocket mutants of myoglobin based on resonance Raman spectroscopy. Biochemistry. 2003; 42:4896–4903. [PubMed: 12718530]
34. Kharitonov VG, Russwurm M, Magde D, Sharma VS, Koesling D. Dissociation of nitric oxide from soluble guanylate cyclase. Biochem Biophys Res Commun. 1997; 239:284–286. [PubMed: 9345311]
35. Sharma VS, Traylor TG, Gardiner R, Mizukami H. Reaction of nitric oxide with heme proteins and model compounds of hemoglobin. Biochemistry. 1987; 26:3837–3843. [PubMed: 3651417]
36. Kharitonov VG, Sharma VS, Magde D, Koesling D. Kinetics of nitric oxide dissociation from five- and six-coordinate nitrosyl hemes and heme proteins, including soluble guanylate cyclase. Biochemistry. 1997; 36:6814–6818. [PubMed: 9184164]
37. Franzen S. Spin-dependent mechanism for diatomic ligand binding to heme. Proc Natl Acad Sci U S A. 2002; 99:16754–16759. [PubMed: 12477933]
38. Strickland N, Harvey JN. Spin-forbidden ligand binding to the ferrous-heme group: ab initio and DFT studies. J Phys Chem B. 2007; 111:841–852. [PubMed: 17249828]
39. Harvey JN. DFT computation of the intrinsic barrier to CO geminate recombination with heme compounds. J Am Chem Soc. 2000; 122:12401–12402.
40. Ionascu D, Gruia F, Ye X, Yu A, Rosca F, Beck C, Demidov A, Olson JS, Champion PM. Temperature-dependent studies of NO recombination to heme and heme proteins. J Am Chem Soc. 2005; 127:16921–16934. [PubMed: 16316238]
41. Olson JS, Phillips GN Jr. Kinetic Pathways and Barriers for Ligand Binding to Myoglobin. J Biol Chem. 1996; 271:17596. [PubMed: 8663556]
42. Dou Y, Maillett DH, Eich RF, Olson JS. Myoglobin as a model system for designing heme protein based blood substitutes. Biophys Chem. 2002; 98:127–148. [PubMed: 12128195]
43. Eich, RF. Biochemistry and Cell Biology. Rice University; Houston: 1997. Reactions of Nitric Oxide with Myoglobin.
44. Foley, EW. Biochemistry and Cell Biology. Rice University; Houston: 2005. Physiologically Relevant Reactions of Myoglobin and Hemoglobin with NO.
45. Coyle CM, Puranik M, Youn H, Nielsen SB, Williams RD, Kerby RL, Roberts GP, Spiro TG. Activation mechanism of the CO sensor CooA. Mutational and resonance Raman spectroscopic studies. J Biol Chem. 2003; 278:35384–35393. [PubMed: 12796503]
46. Hargrove MS, Barry JK, Brucker EA, Berry MB, Phillips GN Jr, Olson JS, Arredondo-Peter R, Dean JM, Klucas RV, Sarath G. Characterization of recombinant soybean leghemoglobin a and apolar distal histidine mutants. J Mol Biol. 1997; 266:1032–1042. [PubMed: 9086279]
47. Arredondo-Peter R, Hargrove MS, Sarath G, Moran JF, Lohrman J, Olson JS, Klucas RV. Rice hemoglobins. Gene cloning, analysis, and O2-binding kinetics of a recombinant protein synthesized in Escherichia coli. Plant Physiol. 1997; 115:1259–1266. [PubMed: 9390447]
48. Lu C, Egawa T, Mukai M, Poole RK, Yeh SR. Hemoglobins from Mycobacterium tuberculosis and Campylobacter jejuni: a comparative study with resonance Raman spectroscopy. Methods Enzymol. 2008; 437:255–286. [PubMed: 18433633]
49. Van Doorslaer S, Dewilde S, Kiger L, Nistor SV, Goovaerts E, Marden MC, Moens L. Nitric oxide binding properties of neuroglobin. A characterization by EPR and flash photolysis. J Biol Chem. 2003; 278:4919–4925. [PubMed: 12480932]
50. Abu-Soud HM, Gachhui R, Raushel FM, Stuehr DJ. The ferrous-dioxy complex of neuronal nitric oxide synthase. Divergent effects of L-arginine and tetrahydrobiopterin on its stability. J Biol Chem. 1997; 272:17349–17353. [PubMed: 9211873]
51. Abu-Soud HM, Wu C, Ghosh DK, Stuehr DJ. Stopped-flow analysis of CO and NO binding to inducible nitric oxide synthase. Biochemistry. 1998; 37:3777–3786. [PubMed: 9521697]

52. Franke A, Stochel G, Jung C, Van Eldik R. Substrate binding favors enhanced NO binding to P450cam. J Am Chem Soc. 2004; 126:4181–4191. [PubMed: 15053607]
53. Gerber NC, Sligar SG. Catalytic mechanism of cytochrome P-450: evidence for a distal charge relay. J Am Chem Soc. 1992; 114:8742–8743.
54. Sevrioukova IF, Peterson JA. Reaction of carbon monoxide and molecular oxygen with P450terp (CYP108) and P450BM-3 (CYP102). Arch Biochem Biophys. 1995; 317:397–404. [PubMed: 7893155]
55. Quaroni LG, Seward HE, McLean KJ, Girvan HM, Ost TW, Noble MA, Kelly SM, Price NC, Cheesman MR, Smith WE, Munro AW. Interaction of nitric oxide with cytochrome P450 BM3. Biochemistry. 2004; 43:16416–16431. [PubMed: 15610036]
56. Lambeir AM, Dunford HB. Oxygen binding to dithionite-reduced chloroperoxidase. Eur J Biochem. 1985; 147:93–96. [PubMed: 3971978]
57. Lange R, Heiber-Langer I, Bonfils C, Fabre I, Negishi M, Balny C. Activation volume and energetic properties of the binding of CO to hemoproteins. Biophys J. 1994; 66:89–98. [PubMed: 8130349]
58. Yeh HC, Hsu PY, Tsai AL, Wang LH. Spectroscopic characterization of the oxyferrous complex of prostacyclin synthase in solution and in trapped sol-gel matrix. FEBS J. 2008; 275:2305–2314. [PubMed: 18397321]
59. Yeh HC, Hsu PY, Wang JS, Tsai AL, Wang LH. Characterization of heme environment and mechanism of peroxide bond cleavage in human prostacyclin synthase. Biochim Biophys Acta. 2005; 1738:121–132. [PubMed: 16406803]
60. Coletta M, Ascoli F, Brunori M, Traylor TG. pH dependence of carbon monoxide binding to ferrous horseradish peroxidase. J Biol Chem. 1986; 261:9811–9814. [PubMed: 3733695]
61. Rodriguez-Lopez JN, Smith AT, Thorneley RN. Effect of distal cavity mutations on the binding and activation of oxygen by ferrous horseradish peroxidase. J Biol Chem. 1997; 272:389–395. [PubMed: 8995273]
62. Abu-Soud HM, Hazen SL. Interrogation of heme pocket environment of mammalian peroxidases with diatomic ligands. Biochemistry. 2001; 40:10747–10755. [PubMed: 11535049]
63. Galijasevic S, Saed GM, Diamond MP, Abu-Soud HM. High dissociation rate constant of ferrous-dioxy complex linked to the catalase-like activity in lactoperoxidase. J Biol Chem. 2004; 279:39465–39470. [PubMed: 15258136]
64. Babcock GT, Wikstrom M. Oxygen activation and the conservation of energy in cell respiration. Nature. 1992; 356:301–309. [PubMed: 1312679]
65. Mims MP, Porras AG, Olson JS, Noble RW, Peterson JA. Ligand binding to heme proteins. An evaluation of distal effects. J Biol Chem. 1983; 258:14219–14232. [PubMed: 6643477]
66. Jantschko W, Furtmuller PG, Zederbauer M, Jakopitsch C, Obinger C. Kinetics of oxygen binding to ferrous myeloperoxidase. Arch Biochem Biophys. 2004; 426:91–97. [PubMed: 15130787]
67. Murphy EJ, Marechal A, Segal AW, Rich PR. CO binding and ligand discrimination in human myeloperoxidase. Biochemistry. 2010; 49:2150–2158. [PubMed: 20146436]
68. Collman JP, Boulatov R, Sunderland CJ, Fu L. Functional analogues of cytochrome c oxidase, myoglobin, and hemoglobin. Chem Rev. 2004; 104:561–588. [PubMed: 14871135]
69. Collman JP, Reed CA. Syntheses of ferrous-porphyrin complexes. A hypothetical model for deoxymyoglobin. J Am Chem Soc. 1973; 95:2048–2049. [PubMed: 4689928]
70. Ford PC, Lorkovic IM. Mechanistic aspects of the reactions of nitric oxide with transition-metal complexes. Chem Rev. 2002; 102:993–1018. [PubMed: 11942785]
71. Tani F, Matsu-ura M, Ariyama K, Setoyama T, Shimada T, Kobayashi S, Hayashi T, Matsuo T, Hisaeda Y, Naruta Y. Iron twin-coronet porphyrins as models of myoglobin and hemoglobin: amphibious electrostatic effects of overhanging hydroxyl groups for successful CO/O2 discrimination. Chemistry. 2003; 9:862–870. [PubMed: 12584701]
72. Chang CK, Traylor TG. Kinetics of oxygen and carbon monoxide binding to synthetic analogs of the myoglobin and hemoglobin active sites. Proc Natl Acad Sci U S A. 1975; 72:1166–1170. [PubMed: 1055374]

73. Collman JP, Brauman JI, Iverson BL, Sessler JL, Morris RM, Gibson QH. O2 and CO binding to iron(II) porphyrins: a comparison of the “picket fence” and “pocket” porphyrins. J Am Chem Soc. 1983; 105:3052–3064.

74. Shantha D, James BR, Dolphin D, Traylor TG, Lopez MA. Dioxygen and carbon monoxide binding to apolar cyclophane hemes: durene-capped hemes. J Am Chem Soc. 1994; 116:6–14.

75. Tetreau C, Lavalette D, Momenteau M, Fischer J, Weiss R. Structure-reactivity relationship in oxygen and carbon monoxide binding with some heme models. J Am Chem Soc. 1994; 116:11840–11848.

76. Smagghe BJ, Halder P, Hargrove MS. Measurement of distal histidine coordination equilibrium and kinetics in hexacoordinate hemoglobins. Methods Enzymol. 2008; 436:359–378. [PubMed: 18237643]

77. Eich RF, Li T, Lemon DD, Doherty DH, Curry SR, Aitken JF, Mathews AJ, Johnson KA, Smith RD, Phillips GN Jr, Olson JS. Mechanism of NO-induced oxidation of myoglobin and hemoglobin. Biochemistry. 1996; 35:6976–6983. [PubMed: 8679521]

78. Gardner PR, Gardner AM, Brashear WT, Suzuki T, Hvitved AN, Setchell KD, Olson JS. Hemoglobins dioxygenate nitric oxide with high fidelity. J Inorg Biochem. 2006; 100:542–550. [PubMed: 16439024]

79. Tsai AL, Berka V, Sharina I, Martin E. Dynamic ligand exchange in soluble guanylyl cyclase: implications for sGC regulation and desensitization. J Biol Chem. 2011

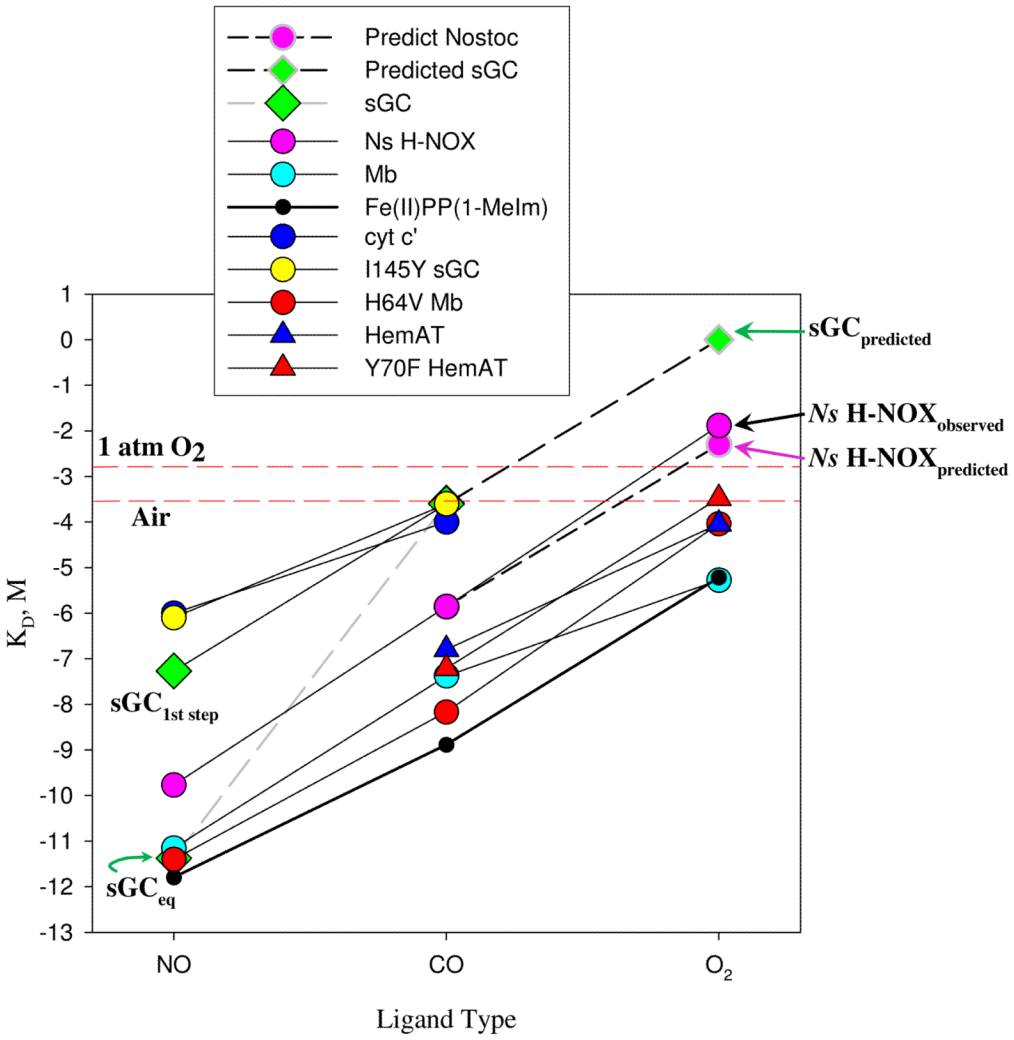

Fig. 1.

"Sliding-scale rule" relationship of the dissociation equilibrium constants, K_D, of various heme sensors. Fe(II)PP(1-MeIm) (black circles and red line); Mb (cyan circles); H64V Mb (red circles); *Ns* H-NOX (pink circles); cyt c′ (blue circles); I145Y sGC (yellow circles); HemAT (blue triangles); Y70F HemAT (red triangles); and sGC (green diamonds) are included for comparison. Predicted $K_D(O_2)$ for sGC and *Ns* H-NOX were obtained by drawing parallel lines from the K_D(CO) to that of the heme model (black dashed lines and symbols with gray edge). The ~4 order difference of K_D(NO) between the 6c and final equilibrium 5c NO complexes formed in sGC were labeled by text and connected to K_D(CO) (solid vs. dotted line) in the figure.

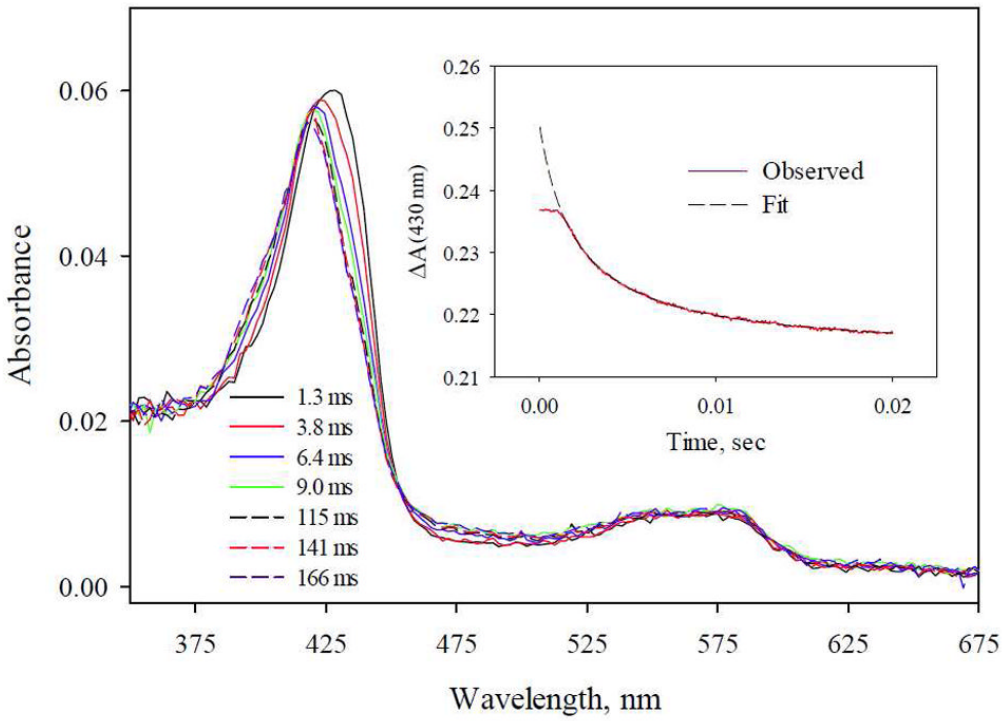

Fig. 2.

Time-dependent optical spectra of the reaction between 1 μM sGC and 1 μM NO (before mixing) at 23 °C recorded in the anaerobic rapid-scan stopped-flow. Spectra were recorded at 1.3 to 166 ms as indicated. Kinetic data of single-wavelength absorbance changes at 430 nm was also recorded (red trace in the Inset) and fitted to a true second-order function (black dash in the Inset) to obtain the rate constant.

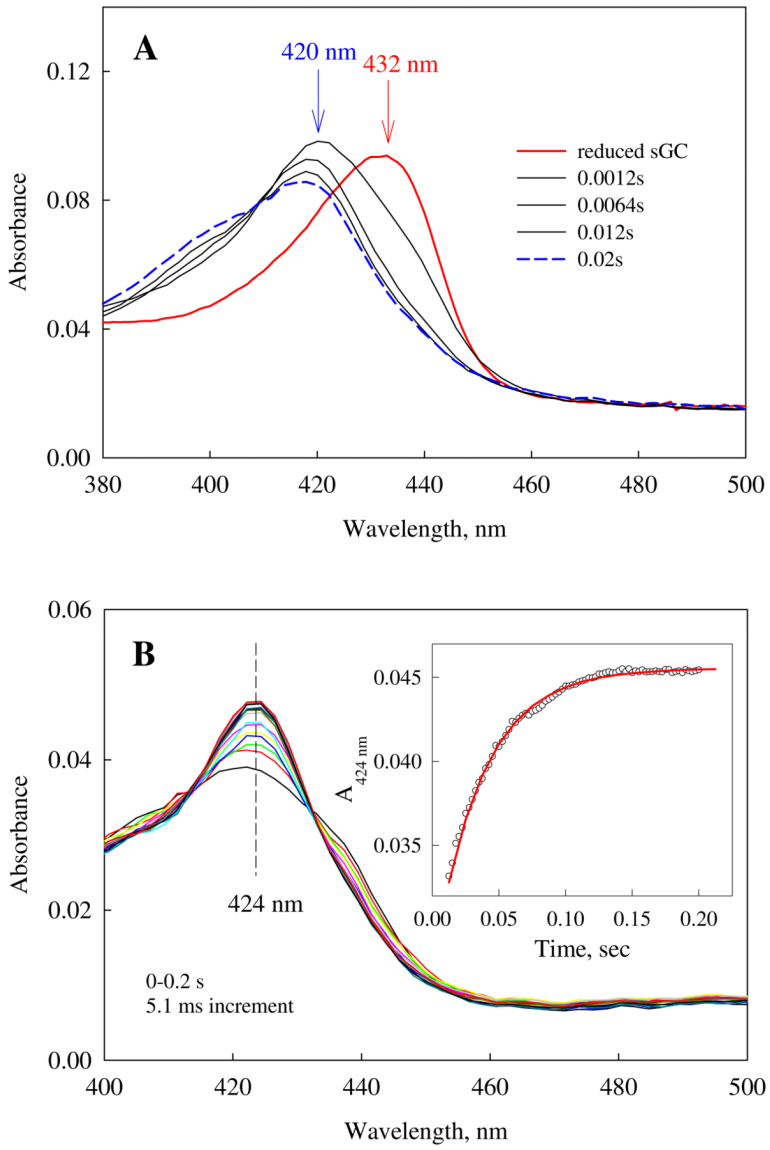

Fig. 3.

(A) Optical spectral changes during the reaction between sGC and stoichiometric amount of NO. Rapid-scan stopped-flow at 23 °C between 3.5 μM Fe(II) sGC and stoichiometric NO was recorded. The peak of Fe(II), 6c NO complex and 5c NO complex are indicated. (B). Optical spectral changes upon reaction between 2 μM sGC (premixed with stoichiometric NO) and 1 mM CO + 25 mM dithionite to determine the k_{off} (NO) from the 6c-NO complex. Kinetic data at 424 nm changes with 20 ms aging time are shown in the Inset.

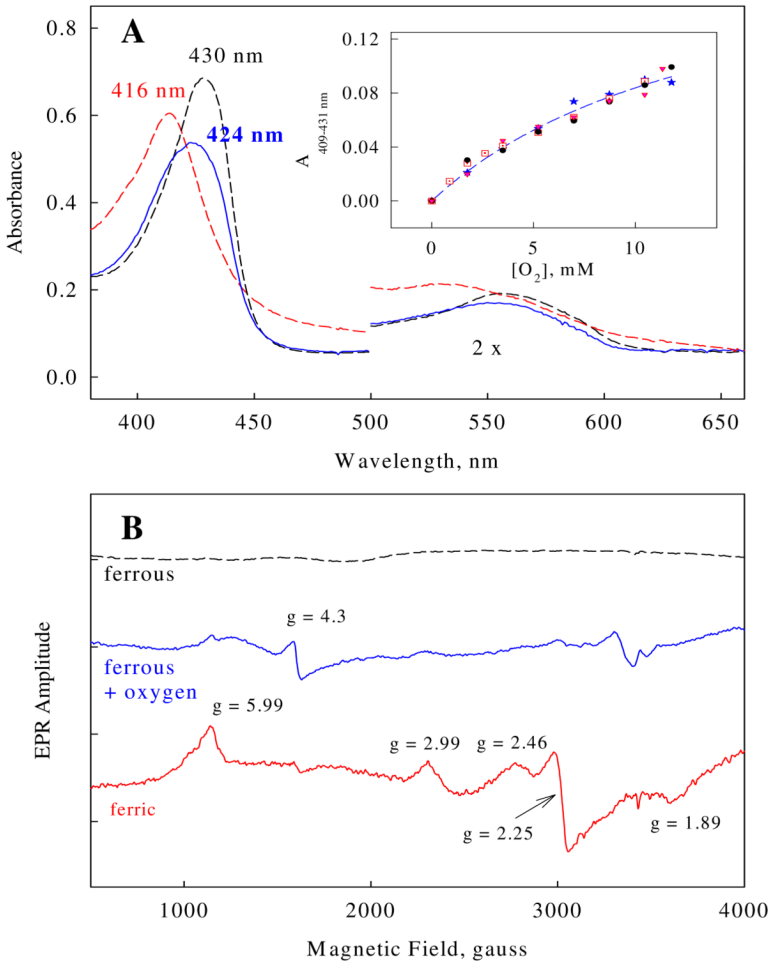

Fig. 4.

(A) Optical spectra of the ferric (red dash), ferrous (black dash) *Ns* H-NOX and ferrous *Ns* H-NOX under 135 psi of O_2 recorded in a high-pressure cell as at 23 °C as described in the Methods. (B) EPR spectra of ferric, ferrous and the oxygen-treated ferrous sample in (A) after open to the air and transferred into EPR tube. All samples are at 50 μM. EPR was recorded at 10K and the EPR condition is described in the Methods.

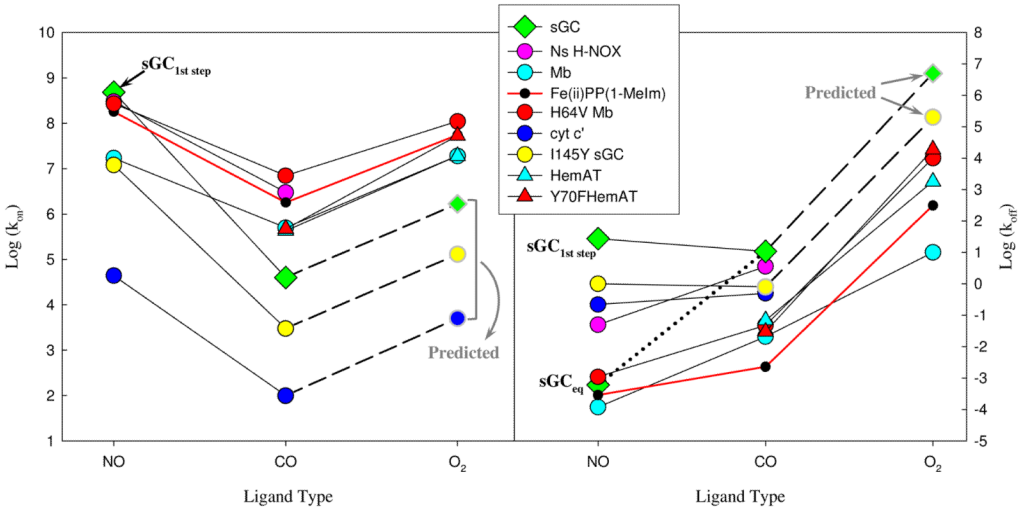

Fig. 5.

Relationship between the k_{on} (or k_{off}), in logarithm, of various heme sensors with three ligand types. The predicted k_{on} (or k_{off}) were shown by dashed lines and symbols with gray edge. Other features match those in Fig. 1.

Fig. 6A.

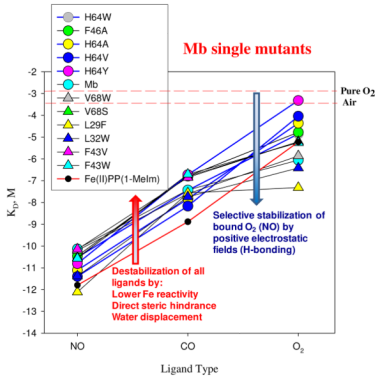

Fig. 6B.

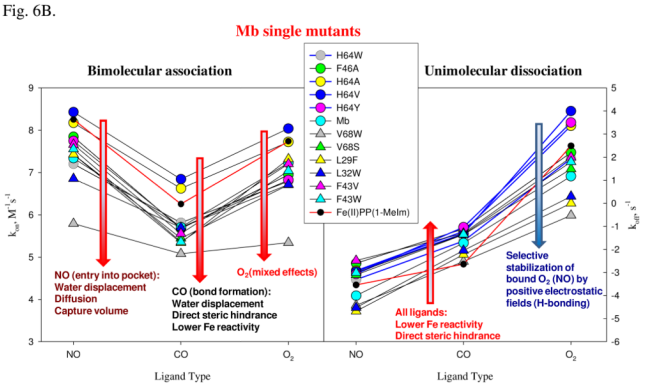

Fig. 6.

Categorical plot between either log K_D (A) or k_{on}/k_{off} and ligand type (B) similar to Fig. 1 was done for a panel of single mutant of Mb together with the model heme control (red line and black circles). Blue thick lines indicate the data of mutants with the key His64 changed to other residues. Binding parameter values are summarized in Table S1 in the Supplementary Information.

Fig. 7A.

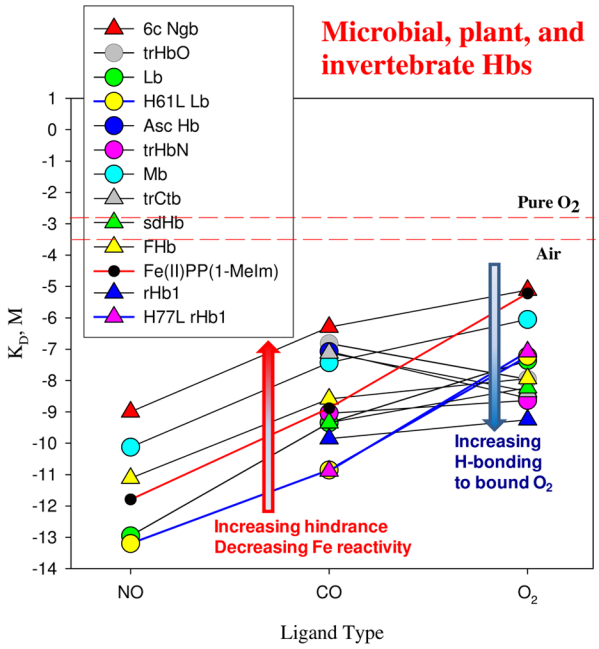

Fig. 7B.

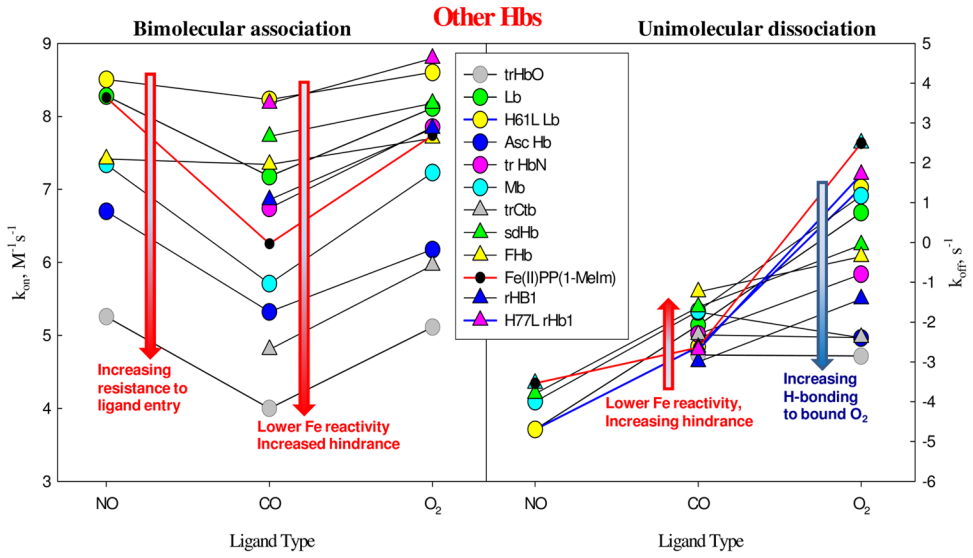

Fig. 7.

Categorical plot between either log K_D (A) or k_{on}/k_{off} and ligand type (B) conducted for several globins: leghemoglobin (Lb, green circles) and its H61L mutant (yellow circles); rice hemoglobin type 1(rHb1blue triangles) and its H77L mutant (red triangles); Hb from *Ascaris suum* (Asc Hb, blue circles); flavohemoglobin (FHb, yellow triangles) from bacteria and fungi; truncated Hb (trHb) from microorganisms including trHbN (pink circles) and trHbO (grey circles) from *Mycobacterium tuberculosis*, trCtb (grey triangles) and sdHb (green triangles) from *Campylobacter jejuni*; and even the six-coordinated neuroglobin (Ngb, red triangles) together with Mb (cyan circles) and the model heme control (red line and black circles). Blue thick lines indicate the data of mutants with the key His64 changed

to other residues. Binding parameter values are summarized in Table S2 in the Supplementary Information.

Fig. 8A.

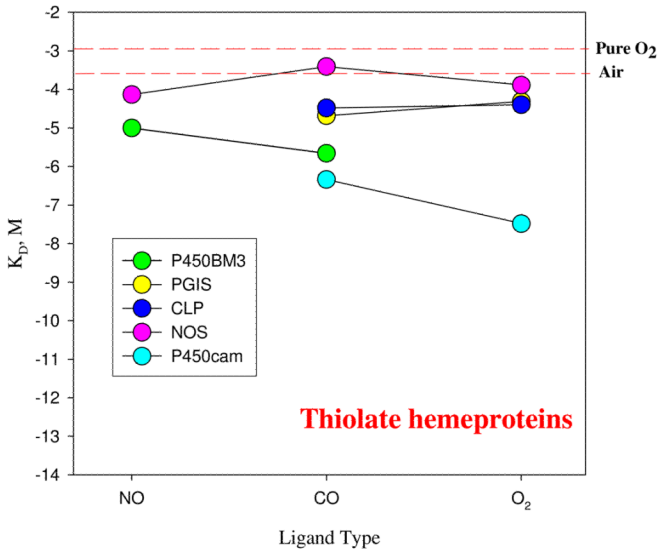

Fig. 8B.

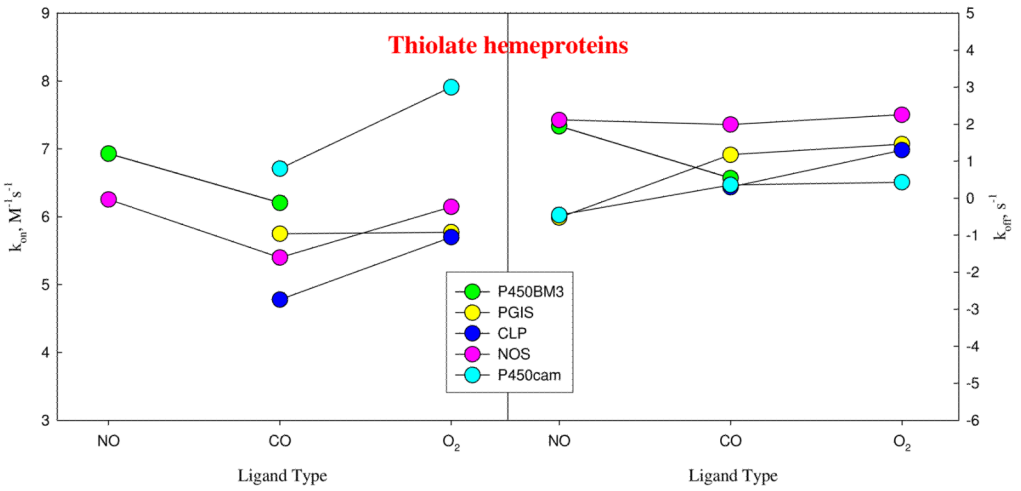

Fig. 8.

Categorical plot between either log K_D (A) or k_{on}/k_{off} and ligand type (B) for several hemeproteins containing a thiolate proximal ligand including: cytochrome P450BM3 (Green circles); prostacyclin synthase (PGIS, yellow circles); chloroperoxidase (CLP, blue circles); nitric oxide synthase (NOS, pink circles); and P450cam. Binding parameter values are summarized in Table S3 in the Supplementary Information.

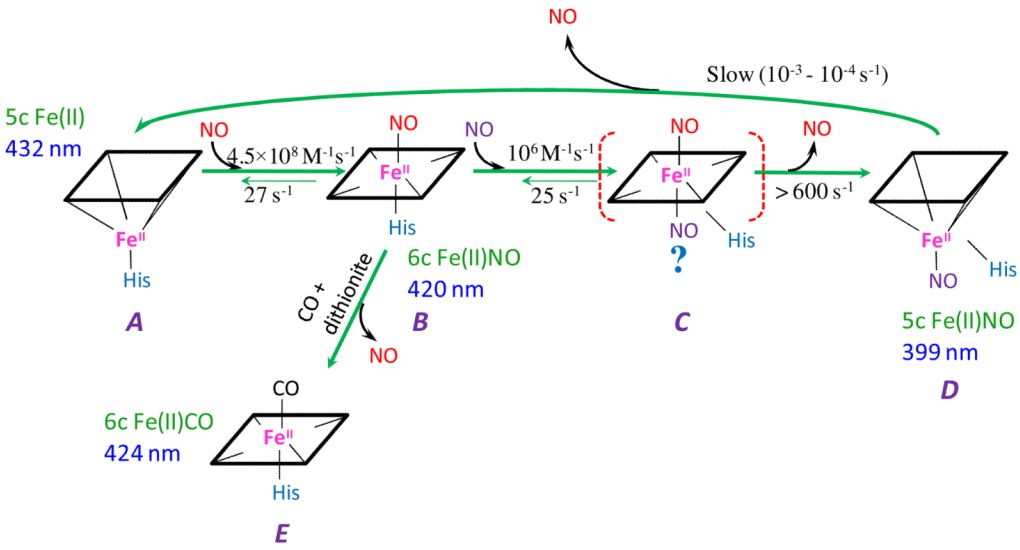

Scheme 1.

Mechanism of multiple step interaction between NO and sGC.

Heme coordination structures and absorption maxima of 6c CO complex (E) formed in excess CO and dithionite, starting 5c Fe(II) sGC (A), 6c NO complex (B), 5c NO complex at final equilibrium (D) are shown. The proposed transient 6c bis-NO complex (C, in bracket) is supported by the [NO]-dependence of the conversion from B → D and recent $^{15}NO/^{14}NO$ ligand binding EPR study (Martin et al., manuscript in revision). Numbers are rate constants at 24 °C determined in this study and one other recent sGC study (79)

Table 1

Gaseous ligand binding parameter values for sGC, αβI145YsGC, cytochrome c′, *NS* H-NOX, HemAT, Mb, H64V Mb and heme model.

Sample	K_D (M)	k_{off}, (s^{-1})	k_{on}, ($M^{-1}s^{-1}$)	[a] Ref. and comments
Wild type sGC:				
NO	[b] 4.2×10^{-12}, [c] 5.4×10^{-8}	6×10^{-4}, [c] ~50[(d)]	1.4×10^{8}, [c] 4.8×10^{8} 2.4×10^{5}[(d)], 1×10^{6}[(e)]	(8, 9, 22), 4 °C [(d)] (8), 4 °C, [(e)] (9)
CO	2.6×10^{-4}	10.7	4×10^{4}	(9, 20, 21)
O_2	N/A	N/A	N/A	(21)
Cytochrome c′:				
NO	1.2 to 9.1×10^{-6}	N/D	4.4×10^{4}	(24, 25, 27)
CO	2.8×10^{-4}	0.028	101	(23, 26)
O_2	N/A	N/A	N/A	
αβI145Y sGC:				
NO	$\leq 0.8\times10^{-6}$	≤ 10	1.2×10^{7}	(9)
CO	2.5×10^{-4}	0.8	3×10^{3}	(9)
O_2	N/A	N/A	N/A	(9)
NS H-NOX				
NO	1.7×10^{-10}	0.05	3×10^{8}	1st 6C-NO complex (13)
	0.8×10^{-6}	1.9	2.4×10^{6}	2nd 6C-NO complex (13)
CO	1.4×10^{-6}	3.6	3×10^{6}	6C-NO complex (13)
O_2	[f] 1.3×10^{-2}	N/A	N/A	Slow autooxidation (13)
HemAT				
NO	-	-	-	
CO	1.6×10^{-7}	7.0×10^{-2}	4.3×10^{5}	(28)
O_2	9.1×10^{-5}	1800	1.9×10^{7}	(28)
Y70FHemAT				
NO	-	-	-	
CO	6.2×10^{-8}	3.0×10^{-2}	4.7×10^{5}	(28)
O_2	3.3×10^{-4}	19000	5.3×10^{7}	(28)
Mb(II), whale:				
NO	4.5×10^{-12}	1.0×10^{-4}	2.2×10^{7}	(18, 19)
CO	3.7×10^{-8}	1.9×10^{-2}	5.1×10^{5}	(17, 18)
O_2	0.9×10^{-6}	15	1.7×10^{7}	(17, 18)
H64V Mb				
NO	4.0×10^{-12}	1.1×10^{-3}	2.7×10^{8}	(3, 18)
CO	6.8×10^{-9}	4.8×10^{-2}	7.0×10^{6}	(3, 18)

Sample	K_D (M)	k_{off}, (s^{-1})	k_{on}, ($M^{-1}s^{-1}$)	[a] Ref. and comments
O_2	9.1×10^{-5}	10000	1.1×10^{8}	(3, 18)
Fe(II)PP(1-MeIm):				
NO	1.6×10^{-12}	2.9×10^{-4}	1.8×10^{8}	(14, 16)
CO	1.3×10^{-9}	2.3×10^{-3}	1.8×10^{6}	(14, 16)
O_2	0.6×10^{-5}	310	5.5×10^{7}	(15)

[a] – Unless otherwise specified, the experimental temperature was 20 – 25 °C.

[b] -- Calculated as k_{off}/k_{on} using values from ref. (8, 34), N/A –not applicable, N/D – not determined.

[c] – Calculated based on the k_{off} and k_{on} for 6c NO complex determined in this study at 24 °C.

[f] – Determined by oxygen binding isotherm under high pressure in this study.